

Room temperature control of skyrmion bubbles stability and switching

M. Schott^{1,2,3,4}, A. Bernand-Mantel^{1,2}, L. Ranno^{1,2}, S. Pizzini^{1,2}, J. Vogel^{1,2}, H. Béa^{1,3,4}, C. Baraduc^{1,3,4}, S. Auffret^{1,3,4}, G. Gaudin^{1,3,4} and D. Givord^{1,2}

¹ Univ. Grenoble Alpes, F-38042 Grenoble, France

² CNRS, Institut NEEL, F-38042 Grenoble, France

³ CNRS, SPINTEC, F-38042 Grenoble, France

⁴ CEA, INAC-SPINTEC, F-38042 Grenoble, France

Skyrmions are nanoscale swirling spin textures stabilized by the Dzyaloshinskii-Moriya interaction, an antisymmetric exchange interaction induced by spin-orbit coupling in presence of broken inversion symmetry. These magnetic structures possess several properties that make them attractive candidates for future spintronics applications. In particular, much lower current density is sufficient to move them as compared to straight domain walls. The use of skyrmions as information carriers demands a control of their individual creation, annihilation and manipulation, with minimal energy consumption. A first step towards applications has been recently achieved with the observation of skyrmions in conventional ultra-thin ferromagnetic transition metal films at room temperature and their manipulation using an electrical current. However, their local creation and annihilation, involves so far solutions that are either energy consuming or difficult to integrate. Here, we demonstrate the reproducible and controlled nucleation and annihilation of skyrmions using electric field gating, an energy efficient and easily integrable solution.

Magnetic skyrmions were studied theoretically more than two decades ago¹⁻³ and first observed at low temperature in the form of hexagonal lattices in non-centrosymmetric crystals⁴⁻⁸ and magnetic multilayers^{9,10}. In the latter case, interfacial Dzyaloshinskii-Moriya interaction (DMI) is induced by symmetry breaking at the interface^{11,12} and enhanced by the very large surface/volume ratio of the ultrathin ferromagnetic layer. Such multilayers, with adjustable magnetic properties, are providing model systems where skyrmion size and stability can be engineered. Recently several groups have reported

the observation of skyrmions at room temperature (RT) in conventional transition-metal-based magnetic multilayers^{13–20}. In some systems, the skyrmions present relatively large dimensions ($\sim 1 \mu\text{m}$) and are more accurately called ‘skyrmion bubbles’. While classical bubbles are stabilized by demagnetizing energy, a skyrmion bubble is stabilized by both DMI and demagnetizing energies. Another difference between classical bubbles and skyrmionic bubbles is their particular symmetry induced by DMI which allows their current driven motion via spin-orbit torques^{13,15,19,20}. This discovery has triggered a growing interest for the use of skyrmions as building blocks for magnetic memories^{21–27} which is reminiscent of the extensive research on magnetic bubble memories in the 1970s²⁸. Such applications will require to create, delete and move skyrmions. The recent observation of current induced displacement of skyrmion bubbles using relatively low current densities reported at RT^{15,19,20,29} is very promising. The creation and annihilation of skyrmions have been addressed theoretically^{23,30,31} and experimentally^{32–34} by different techniques such as spin transfer torque^{23,31,32}, heat^{30,35} and strain³⁴. However, those techniques are either energy consuming or difficult to integrate in functional devices. In analogy to what has been developed to switch small ferromagnetic elements³⁶, the use of electric field gating to manipulate skyrmions offers several advantages: the low power consumption, the possibility to act locally and an easy integration. Furthermore, a major issue of current induced nucleation, namely, unwanted current displacement of skyrmions during the writing process, is naturally absent using electric field writing. Those advantages have motivated some theoretical works concerning the electric control of skyrmions^{26,37}. The only experimental attempt for skyrmion electrical switching has been carried out in an epitaxial material and at low temperature³³. In this letter, we report on the observation of thermally activated nucleation and annihilation of magnetic skyrmion bubbles at RT and we demonstrate the possibility to electrically switch them on and off under a constant biasing magnetic field.

We have selected for this study the *Pt/Co/oxide* system, for which a large DMI value has been reported^{38–41}. To demonstrate the electrical switching of skyrmions we have chosen *Co* thicknesses close to the spin reorientation transition, for which enhanced electric field effects have been observed^{42,43}. The *Co* layer presents a thickness gradient which is created by the oxidation of a wedge shaped *Al* top layer (see Fig. 1b). A high-k *HfO₂* dielectric layer and a transparent top Indium Tin oxide (*ITO*) electrode have been deposited on top of the *Pt/Co/oxide* trilayer, allowing magnetic characterization using magneto-optical Kerr effect under an applied electric field.

Characterisation of the labyrinthine state

The magnetic domains are imaged at RT using a Kerr microscope in polar geometry. At low magnetic field a labyrinthine demagnetized state is observed (Fig. 1a). The formation of labyrinthine domains is the consequence of a balance between competing energies: the demagnetizing energy and the domain wall (DW) energy. A variation of the labyrinthine domain width L is observed along the wedge direction (Fig. 1c). To understand this variation we have used an analytical model^{44,45} describing for ultrathin films the labyrinthine domain width $L = \alpha \cdot t \cdot \exp(\pi L_0/t)$ as function of the saturation magnetization M_S , the DW energy σ_W , the magnetic film thickness t , the characteristic dipolar length $L_0 = \sigma_W/\mu_0 \cdot M_S^2$ and α a numerical constant (see Methods). The experimental value of the DW energy σ_W can be calculated from this equation with the measured values of L , t and M_S (see supplementary S1-S3). At position p_0 , $L = 2.9 \mu\text{m}$, $t = 0.47 \text{ nm}$, $M_S = 0.93 \text{ MA/m}$ and we find $\sigma_W = 1.44 \text{ mJ/m}^2$. This value can be compared to the classical Bloch wall energy $\sigma_W^{Bloch} = 4\sqrt{A_{ex}K_{eff}}$. Using the experimental effective anisotropy value $K_{eff} = 0.28 \text{ MJ/m}^3$ (see supplementary S4) and an exchange constant A_{ex} in the $5 - 15 \text{ pJ/m}$ range we find $\sigma_W^{Bloch} = 5 - 8 \text{ mJ/m}^2$ which is much larger than the experimental DW energy. The deviation of the from the Bloch formula can be explained by the presence of interfacial DMI in the trilayer which reduces σ_W according to the expression^{19,46}: $\sigma_W = 4\sqrt{A_{ex}K_{eff}} - \pi D$ where D is the DMI energy in mJ/m^2 . We deduce a DMI term $D = 1 - 2 \text{ mJ/m}^2$ which is consistent with the values obtained in similar *Pt/Co/oxide* trilayers³⁸⁻⁴¹. The low DW energy in our system is at the origin of the observed spontaneous demagnetization of the layer at RT on a few second timescale. This thermally activated demagnetization is due to a combination of spontaneous nucleation of magnetic domains and thermally activated motion of domain walls under zero applied magnetic field (see supplementary S5). Such thermal movement of labyrinthine magnetic domains has been reported previously in ultrathin films where the DW energy was lowered by the proximity of the spin reorientation transition^{47,48}. This DW mobility, in combination with the high nucleation rate, allows reaching an equilibrium demagnetized state in a few seconds in the major part of the diagram of Fig. 1a (between p_0 and p_3). Above p_0 , the demagnetized state starts to derive from the equilibrium one and we decide not to extract the domain width in this region. We now discuss the origin of the decrease by a factor of 3 of the domain width L along the wedge (Fig. 1c). The *Co* thickness t variation is of the order of 1% along the considered region of $500 \mu\text{m}$ length and is negligible compared to the variation of the other parameters. However, as t decreases a diminution of M_S by 8.4% is observed (see supplementary S3). According to its analytical expression, the domain width L should increase when M_S , and thus the demagnetizing energy, decreases. However, the

opposite is observed in Fig. 1c. We deduce that a strong decrease of the DW energy, over-compensating the M_s variation is at the origin of the decrease of L . If we assume a constant DMI term, the variation of the DW energy $\sigma_w = 4\sqrt{A_{ex}K_{eff}} - \pi D$ must be related to A_{ex} and K_{eff} variations. This is confirmed by our experimental observations: a reduction of K_{eff} with t is measured (see supplementary S4) and a diminution of A_{ex} is expected from the M_s decrease with $t^{49,50}$.

Observation of skyrmion bubbles

When a perpendicular magnetic field larger than 0.1 mT is applied, micron-sized bubbles appear (Fig. 1a). This transition from a labyrinthine pattern into a bubble lattice with applied magnetic field is unusual for a classical bubble system. In the classical case the magnetic domains should shrink in width and length but the number of magnetic objects should remain constant⁴⁴, leaving very few bubbles. This situation is observed on the right side of the image in Fig. 1a. As we go from right to left, the increasing density of bubbles domains indicates the presence of thermally activated nucleation. This thermally activated process is enabled by the reduction of the DW energy σ_w , due to the presence of DMI. This implies a skyrmionic nature of the nucleated bubbles, which is confirmed by the observation of their unidirectional motion against electron flow, as expected for this system (see supplementary S6). To understand the nucleation and stability of the skyrmion bubbles in our system, we have calculated analytically the energy of an isolated skyrmion bubble using a “thin wall” model which is valid for negligible DW width ($\delta_w \sim 10$ nm in our case) compared to the bubble diameter (few μm) (see Methods). The skyrmion bubble energy $E_{sb}(t, M_s, \sigma_w)$ is the sum of DW, Zeeman and demagnetizing terms. The energy of an individual bubble relative to the saturated state can be written as:

$$\Delta E_{sb}(R, t, M_s, \sigma_w) = \sigma_w \cdot t \cdot 2 \cdot \pi \cdot R + 2\mu_0 M_s \cdot H \cdot t \cdot \pi \cdot R^2 - \mu_0 M_s^2 \cdot \pi \cdot t^3 \cdot I(d)$$

where σ_w is the DW energy, t the layer thickness, R the bubble radius, M_s the saturation magnetization, $\mu_0 H$ the applied magnetic field, and $I(d)$ the stray field energy gain where $d = 2R/t$ (see Methods). The skyrmion bubble energy ΔE_{sb} versus the bubble diameter (Fig. 2.g) presents two local extrema. We define the skyrmion bubble nucleation energy E_n as the local maximum and the annihilation energy E_a as the difference between the local maximum and minimum (see Fig. 2.g). The calculated nucleation and annihilation energies are shown in Fig. 1d,e. For this calculation, we have used the M_s , t and σ_w values and their variations along the wedge estimated experimentally using a combination of magneto-optical Kerr and VSM-SQUID magnetometry (see supplementary S1-S3). As our characterization setup

was adapted to study the 100 ms-few second timescale, we draw as a guide to the eye, a white line indicating the RT thermal activation frontier, $E/k_B T_{293K} = 23$ (Neel-Brown model) below which nucleation/annihilation events are occurring at a rate $\Gamma > 1$ Hz. The analytical skyrmion bubble model reproduces several features observed in Fig. 1a. In Fig. 1d, for a constant magnetic field, the increase of the nucleation barrier E_n with the DW energy explains the decrease in the bubble density observed in Fig. 1a as the *Co* gets thicker. In the zone indicated by the number 2 in Fig. 1d, skyrmion bubbles are observed despite the increase of E_n above the thermal activation frontier. Those skyrmion bubbles are metastable skyrmions bubbles nucleated at lower magnetic field or stabilized by local magnetic inhomogeneities, which might locally lower the nucleation barrier. In the position indicated by the number 1 in Fig. 1d,e, both nucleation and annihilation are expected with a rate $\Gamma > 1$ Hz. This thermal instability of the skyrmion bubbles is observed in a time dependent measurement (see supplementary S7). On the contrary, the skyrmion bubbles present a very high thermal stability in a large part of the diagram (below the white line in Fig. 1e). For example, in the middle region, at intermediate magnetic field and DW energy, the annihilation barrier is $E_a/kT > 40$. In this region no annihilation of the skyrmion bubbles is observed up to few minutes timescale. A position p_1 near this region has been selected for the observation of skyrmion bubbles under electric field.

Electric field control of the skyrmion bubbles density

The behavior of skyrmion bubbles under electric field gating is studied through a transparent *ITO* electrode (see Fig. 1b). Polar Kerr images recorded for different applied electric fields are presented in Fig 2 a-c. A variation of the skyrmion bubble density and mean diameter with the electric field is observed (see Fig. 2f). To explain the observed behavior, the analytical skyrmion bubble model described previously is used again. The parameters used for the simulation (t , M_s and σ_w) and the variation of M_s and σ_w with the electric field are determined experimentally (see supplementary S10). When the electric field is switched from -5 V to +5 V, M_s and σ_w vary respectively by 0.09 MA/m and 0.32 mJ/m². These experimental parameters are used in the simulation in Fig. 2g where the energy difference between a saturated state and an isolated bubble is plotted as a function of the bubble diameter. The observed decrease in the skyrmion bubbles number with increasing electric field is consistent with the increase in the nucleation energy barrier E_n combined with a decrease of the annihilation energy barrier E_a obtained in the simulation. In Fig. 2 d,e differential images are shown where the blue/red bubbles correspond to bubbles which have appeared/disappeared. In Fig. 2d, both blue and red bubbles are observed with a

majority of blue bubbles. This is explained by a domination of nucleation processes as $E_n \leq 23 k_B T_{293K}$ and $E_a \geq 23 k_B T_{293K}$ in the -5 V to 0 V range (Fig. 2g). In that voltage range, the continuous nucleation of bubbles causes the displacement of the existing bubbles due to repulsion between bubbles. On the contrary the 0 V to +5 V range is dominated by annihilation processes with $E_a \leq 23 k_B T_{293K}$ and $E_n \geq 23 k_B T_{293K}$ as confirmed by a large majority of red bubbles in Fig. 2e. A small decrease in the bubble diameter with increasing electric field (Fig. 2f) is observed. This decrease can be explained by the increase in σ_w with electric field. However this decrease is small as it is partially compensated by a M_s increase (and consequently a demagnetizing energy increase) which has an opposite effect on the bubble diameter as compared to a DW energy increase. The variation of the bubble-bubble interaction, which is neglected in our model, should also be taken into account. Despite this approximation, our model reproduces well the observed electric field variation of the bubble diameter (Fig. 2g).

Skyrmion bubbles switching

Now that the electric field control of skyrmion bubble density is demonstrated, we carry out the proof of concept of an electrical skyrmion switch by turning the electric field to higher voltages. In Fig. 3a-b, we show the electric field switching from a state with a very high skyrmion bubble density to a state with no skyrmion bubbles. This electric switching of skyrmion bubbles is reversible and reproducible sequentially as we can see in Fig. 3d where the average Kerr intensity is recorded below the electrode as function of time while the voltage is switched between +/-20 V (see supplementary S9). To understand the origin of this switching effect, polar Kerr hysteresis loops with in plane applied magnetic field have been measured to estimate the variation of M_s and K_{eff} under electric field (see supplementary S8). When the voltage varies from +20 V to -20 V, M_s and K_{eff} are modified respectively by -47% and -64%. A variation of D with electric field may also be observed in our experiment as predicted theoretically⁵¹, but the detailed analysis necessary to separate the D variation from A_{ex} , M_s and K_{eff} is beyond the scope of this study. We deduce from $K_{eff} = K_s/t - 1/2\mu_0 M_s^2$ a K_s variation $\Delta K_s/\Delta E = 810 \text{ fJ/V/m}$. This strong electric field variations of the magnetic properties are due to a modification of the electron density of state in the *Co* and are most likely enhanced by the proximity of T_c as observed in previous works on *Pt/Co/oxide*⁵² in the ultrathin regime. The short time scale at which the electric field effect is triggered (faster than the few 100 ms time resolution of the present setup) and its volatility, rules out ionic effects⁵³. In addition, no measurable current is passing between the ITO electrode and the metallic multilayer ($R >$

10^{12} Ohm). The variation of the skyrmion bubble energy with electric field (Fig. 3c,d) is calculated using the experimental M_S variations with electric field and a DW energy variation adjusted to fit the observed skyrmion bubble nucleation/annihilation rates (see supplementary S10). For positive voltage, skyrmion bubbles vanish due to a strong increase of the nucleation energy combined with a decrease of the annihilation barrier: nucleation is prevented and annihilation of bubbles can be thermally activated. On the contrary, for negative electric field, the nucleation energy E_n is strongly reduced whereas the annihilation energy barrier becomes very large, thus favoring the creation of stable skyrmion bubbles. Consequently, the electric field can be used to switch skyrmion bubbles on and off in a very efficient way as both E_n and E_a are modified. Comparatively, the magnetic field is less efficient as it strongly affects E_a but has a small effect on E_n (see Fig. 1e). In our system the observed switch effect is associated to strong M_S and σ_W variations only expected near T_C . However, the variation of M_S and σ_W have opposite effects: an increase of M_S/σ_W is decreasing/increasing E_n . Consequently, the skyrmion switch effect should be much more efficient at fixed M_S . To check this we calculated in Fig. 3f the skyrmion bubble energy in the case of a thicker Co layer of 0.6 nm (with a higher T_C), which is expected to show negligible M_S variation with electric field but a significative K_{eff} change⁴². We see that the skyrmion switch effect (i.e. reducing the nucleation barrier and increasing the annihilation barrier) can be efficient at fixed M_S with a σ_W variation as small as 5%. In this case, the skyrmion bubbles are scaled down to a few 100 nm of diameter. Below this size, our thin wall analytical model is no more valid and further simulations are necessary to study the skyrmion switch effect on a nanometer sized skyrmion in a confined geometry.

Conclusion

We have reported the presence at RT of micron sized skyrmion bubbles in a *Pt/Co/oxide* trilayer. The DMI strength, which is of the order of 1-2 mJ/m², reduces the DW energy by a factor of ~ 5 with respect to the classical Bloch case and enables the stabilization of skyrmion bubbles. The observed skyrmion bubbles density variation along the wedge and versus electric field is well described by an analytical isolated bubble model. We demonstrate the efficient and reproducible electric field writing and deleting of skyrmion bubbles via a skyrmion switch effect, which is compatible with energy efficient skyrmion-based applications. These results constitute an important milestone towards the use of skyrmions for memory or logic devices.

Acknowledgement

The authors thanks A. Thiaville, O. Fruchart, M. Chshiev, O. Boulle, I. M. Miron and V. Cros for fruitful discussions. We acknowledge the support from the Nanofab facility and the pôles magnetometrie and ingénierie expérimentale from Institut Néel. We thank L. Cagnon for ALD deposition.

Author contributions

A. B-M., G. G. and D. G. conceived the original idea. M. S. and S. A. fabricated the sample. M. S. and A. B.-M. performed the experiments. M. S., A. B-M., L. R., S. P., J. V., H. B. and C. B. analysed the data and discussed the results. A. B-M. wrote the paper, and all authors provided feedback.

Competing financial interests

The authors declare no competing financial interests.

Corresponding author

Correspondence to: anne.bernard-mantel@neel.cnrs.fr

Methods

Sample preparation

The $Pt(3\text{ nm})/Co(0.6\text{ nm})/Al 0.76\text{ nm}$ to $Al 1.76\text{ nm}$ film was deposited by magnetron sputtering on a Si wafer with a $\sim 500\text{ nm}$ thick thermal SiO_2 top layer. The Al layer was oxidized in-situ by a O_2 plasma. A $\sim 90\text{ nm}$ HfO_2 layer is deposited ex-situ by Atomic Layer Deposition. Indium Tin oxide electrodes deposited by sputtering where patterned by lift-off in the form of $50 \times 800\text{ }\mu\text{m}$ rectangles.

Analytical model of the labyrinthine domains width

The theoretical labyrinthine domain width L has been calculated using a parallel band domains model in the case where the domain width is negligible compared to the DW width. In the case of ultra-thin films, when the thickness is much smaller than the characteristic dipolar length^{45,54} : $t \ll L_0$ with $L_0 = \sigma_W/\mu_0 \cdot M_s^2$ where M_s is the saturation magnetization and σ_W the domain wall energy, the domain width L can be written as $L = \alpha \cdot t \cdot \exp(\pi L_0/t)$ where t is the magnetic film thickness and α a constant $\alpha = \exp(\frac{\pi b}{2} + 1) \sim 0.955$ where b is the numerical evaluation of a series⁴⁵. Using this expression we obtain the domain wall energy $\sigma_W = \ln(L/(\alpha \cdot t)) \cdot \mu_0 \cdot M_s^2 \cdot t / \pi$.

Analytical “thin wall” bubble model

We have used an analytical formula to approximate the energy of an individual bubble of radius r relative to the saturated state^{28,55}. The model used here is valid for $Q = K_u/K_d > 1$, where K_u is the effective uniaxial out of plane anisotropy and K_d the demagnetizing energy. In our case we have $Q = 0.82/0.54 = 1.52$. It was shown that this standard theory is well applicable for $Q > 1.5$. The energy of an individual bubbles relative to the saturated state can be written as:

$$\Delta E_{sb} = \sigma_w \cdot t \cdot 2 \cdot \pi \cdot R + 2\mu_0 M_s \cdot H \cdot t \cdot \pi \cdot R^2 - \mu_0 M_s^2 \cdot \pi \cdot t^3 \cdot I(d)$$

where σ_w is the DW energy, t the layer thickness, R the bubble radius, M_s the saturation magnetisation, $\mu_0 H$ the applied magnetic field, and $I(d)$ defined as follow:

$$I(d) = -\frac{2}{3\mu} d [d^2 + (1 - d^2)E(u^2)/u - K(u^2)/u]$$

where $d = 2R/t$, $u^2 = d^2/(1 + d^2)$ and $E(u)$ and $K(u)$ are elliptic integrals defined as:

$$E(u) = \int_0^{\pi/2} \sqrt{1 - u \cdot \sin^2(\alpha)} d\alpha \text{ and } K(u) = \int_0^{\pi/2} d\alpha / \sqrt{1 - u \cdot \sin^2(\alpha)}$$

References

1. Ivanov, B. a., Stephanovich, V. a. & Zhmudskii, a. a. Magnetic vortices □ The microscopic analogs of magnetic bubbles. *J. Magn. Magn. Mater.* **88**, 116–120 (1990).
2. Bogdanov, a & Hubert, a. The properties of isolated magnetic vortices. *Phys. Status Solidi* **186**, 527–543 (1994).
3. Abanov, A. & Pokrovsky, V. L. Skyrmion in a real magnetic film. *Phys. Rev. B* **58**, 4 (1998).
4. Yu, X. Z. Real-space observation of a two-dimensional skyrmion crystal. *Nature* **465**, 901–904 (2010).
5. Tonomura, A. Real-space observation of skyrmion lattice in helimagnet MnSi thin samples. *Nano Lett.* **12**, 1673–1677 (2012).
6. Mühlbauer, S. Skyrmion lattice in a chiral magnet. *Science (80-.)* **323**, 915–919 (2009).
7. Munzer, W. Skyrmion lattice in the doped semiconductor Fe_{1-x}CoxSi. *Phys. Rev. B* **81**, 41203

(2010).

- 8. Pappas, C. Chiral paramagnetic skyrmion-like phase in MnSi. *Phys. Rev. Lett.* **102**, 197202 (2009).
- 9. Bode, M. Chiral magnetic order at surfaces driven by inversion asymmetry. *Nature* **447**, 190–193 (2007).
- 10. Heinze, S. Spontaneous atomic-scale magnetic skyrmion lattice in two dimensions. *Nat. Phys.* **7**, 713–718 (2011).
- 11. Crépieux, a. & Lacroix, C. Dzyaloshinsky–Moriya interactions induced by symmetry breaking at a surface. *J. Magn. Magn. Mater.* **182**, 341–349 (1998).
- 12. Bogdanov, A. N. & Rößler, U. K. Chiral symmetric breaking in magnetic thin films and multilayers. *Phys. Rev. Lett.* **87**, 37203 (2001).
- 13. Buttner, F. *et al.* Dynamics and inertia of skyrmionic spin structures. *Nat Phys* **11**, 225–228 (2015).
- 14. Chen, G., Mascaraque, A., N'Diaye, A. T. & Schmid, A. K. Room temperature skyrmion ground state stabilized through interlayer exchange coupling. *Appl. Phys. Lett.* **106**, 242404 (2015).
- 15. Jiang, W. *et al.* Blowing magnetic skyrmion bubbles. *Science (80-.)* **349**, 283–286 (2015).
- 16. Moon, K.-W. *et al.* Magnetic bubblecade memory based on chiral domain walls. *Sci. Rep.* **5**, 9166 (2015).
- 17. Boulle, O. *et al.* Room-temperature chiral magnetic skyrmions in ultrathin magnetic nanostructures. *Nat Nano advance on*, (2016).
- 18. Moreau-Luchaire, C. *et al.* Additive interfacial chiral interaction in multilayers for stabilization of small individual skyrmions at room temperature. *Nat Nano* **11**, 444–448 (2016).
- 19. Woo, S. *et al.* Observation of room-temperature magnetic skyrmions and their current-driven dynamics in ultrathin metallic ferromagnets. *Nat Mater* **15**, 501–506 (2016).
- 20. Yu, G. *et al.* Room-Temperature Creation and Spin–Orbit Torque Manipulation of Skyrmions in Thin Films with Engineered Asymmetry. *Nano Lett.* **16**, 1981–1988 (2016).
- 21. Kiselev, N. S., Bogdanov, A. N., Schäfer, R. & Rößler, U. K. Chiral skyrmions in thin magnetic films: new objects for magnetic storage technologies? *J. Phys. D. Appl. Phys.* **44**, 392001+ (2011).
- 22. Fert, A., Cros, V. & Sampaio, J. Skyrmions on the track. *Nat. Nanotech.* **8**, 152–156 (2013).

23. Sampaio, J., Cros, V., Rohart, S., Thiaville, A. & Fert, A. Nucleation, stability and current-induced motion of isolated magnetic skyrmions in nanostructures. *Nat. Nanotech.* **8**, 839–844 (2013).
24. Zhang, X. Skyrmion-skyrmion and skyrmion-edge repulsions in skyrmion-based racetrack memory. *Sci. Rep.* **5**, 7643 (2015).
25. Zhang, X., Ezawa, M. & Zhou, Y. Magnetic skyrmion logic gates: conversion, duplication and merging of skyrmions. *Sci. Rep.* **5**, 9400+ (2015).
26. Kang, W. *et al.* Voltage Controlled Magnetic Skyrmion Motion for Racetrack Memory. *Sci. Rep.* **6**, 23164 (2016).
27. Wiesendanger, R. Nanoscale magnetic skyrmions in metallic films and multilayers: a new twist for spintronics. *Nat. Rev. Mater.* **1**, 16044 (2016).
28. A.H. Bobeck. Properties and device applications of magnetic domains in orthoferrites. *Bell Syst. Tech. J.* **46**, 1901 (1967).
29. Yu, X. Z. *et al.* Skyrmion flow near room temperature in an ultralow current density. *Nat. Commun.* **3**, 988 (2012).
30. Koshibae, W. & Nagaosa, N. Creation of skyrmions and antiskyrmions by local heating. *Nat. Commun.* **5**, (2014).
31. Zhou, Y. *et al.* Dynamically stabilized magnetic skyrmions. *Nat. Commun.* **6**, 8193 (2015).
32. Romming, N. *et al.* Writing and Deleting Single Magnetic Skyrmions. *Science (80-.)* **341**, 636–639 (2013).
33. Hsu, P.-J. *et al.* Electric-field-driven switching of individual magnetic skyrmions. *Nat Nano advance on*, (2016).
34. Nii, Y. *et al.* Uniaxial stress control of skyrmion phase. *Nat. Commun.* **6**, 8539 (2015).
35. Finazzi, M. *et al.* Laser-Induced Magnetic Nanostructures with Tunable Topological Properties. *Phys. Rev. Lett.* **110**, 177205 (2013).
36. Wang, W. G. & Chien, C. L. Voltage-induced switching in magnetic tunnel junctions with perpendicular magnetic anisotropy. *J. Phys. D. Appl. Phys.* **46**, 74004 (2013).
37. Fook, H. T., Gan, W. L. & Lew, W. S. Gateable Skyrmion Transport via Field-induced Potential Barrier Modulation. *Sci. Rep.* **6**, 21099 (2016).
38. Pizzini, S. *et al.* Chirality-Induced asymmetric magnetic nucleation in Pt/Co/AlOx ultrathin

microstructures. *Phys. Rev. Lett.* **113**, 47203 (2014).

39. Vaňatka, M. *et al.* Velocity asymmetry of Dzyaloshinskii domain walls in the creep and flow regimes. *J. Phys. Condens. Matter* **27**, 326002 (2015).

40. Tetienne, J.-P. *et al.* The nature of domain walls in ultrathin ferromagnets revealed by scanning nanomagnetometry. *Nat. Commun.* **6**, 6733 (2015).

41. Belmeguenai, M. *et al.* Interfacial Dzyaloshinskii-Moriya interaction in perpendicularly magnetized Pt/Co/AlO ultrathin films measured by Brillouin light spectroscopy. *Phys. Rev. B* **91**, 1–4 (2015).

42. Bernand-Mantel, A. *et al.* Electric-field control of domain wall nucleation and pinning in a metallic ferromagnet. *Appl. Phys. Lett.* **102**, 122406 (2013).

43. Maruyama, T. *et al.* Large voltage-induced magnetic anisotropy change in a few atomic layers of iron. *Nat. Nanotechnol.* **4**, 158 (2009).

44. Hubert, A. & Schäfer, R. *Magnetic Domains*. (Springer, 1998).

45. Kaplan, B. & Gehring, G. A. The domain structure in ultrathin magnetic films. *J. Magn. Magn. Mater.* **128**, 111 (1993).

46. Heide, M., Bihlmayer, G. & Blugel, S. Dzyaloshinskii-Moriya interaction accounting for the orientation of magnetic domains in ultrathin films: Fe/W(110). *Phys. Rev. B* **78**, 140403 (2008).

47. Won, C. *et al.* Magnetic stripe melting at the spin reorientation transition in Fe Ni Cu(001). *Phys. Rev. B - Condens. Matter Mater. Phys.* **71**, 1–5 (2005).

48. Bergeard, N. *et al.* Dynamic fluctuations and two-dimensional melting at the spin reorientation transition. *Phys. Rev. B - Condens. Matter Mater. Phys.* **86**, 1–5 (2012).

49. Eyrich, C. *et al.* Effects of substitution on the exchange stiffness and magnetization of Co films. *Phys. Rev. B - Condens. Matter Mater. Phys.* **90**, 1–12 (2014).

50. Moreno, R. *et al.* Temperature-dependent exchange stiffness and domain wall width in Co. *Phys. Rev. B* **94**, 104433 (2016).

51. Yang, H., Boulle, O., Cros, V., Fert, A. & Chshiev, M. Controlling Dzyaloshinskii-Moriya Interaction via Chirality Dependent Layer Stacking, Insulator Capping and Electric Field. 14 (2016).

52. Chiba, D. & Ono, T. Control of magnetism in Co by an electric field. *J. Phys. D. Appl. Phys.* **46**, 213001 (2013).

53. Bauer, U., Emori, S. & Beach, G. S. D. Voltage-gated modulation of domain wall creep dynamics in an ultrathin metallic ferromagnet. *Appl. Phys. Lett.* **101**, 172403 (2012).
54. Kooy, C. & Enz, U. Experimental and theoretical study of the domain configuration in thin layers of BaFeO. *Phillips Res. Rept.* **15**, 7 (1960).
55. Malozemoff, A. P. & Slonczewski, J. C. *Magnetic Domain Walls in Bubble Materials*. (Academic Press, 1979).

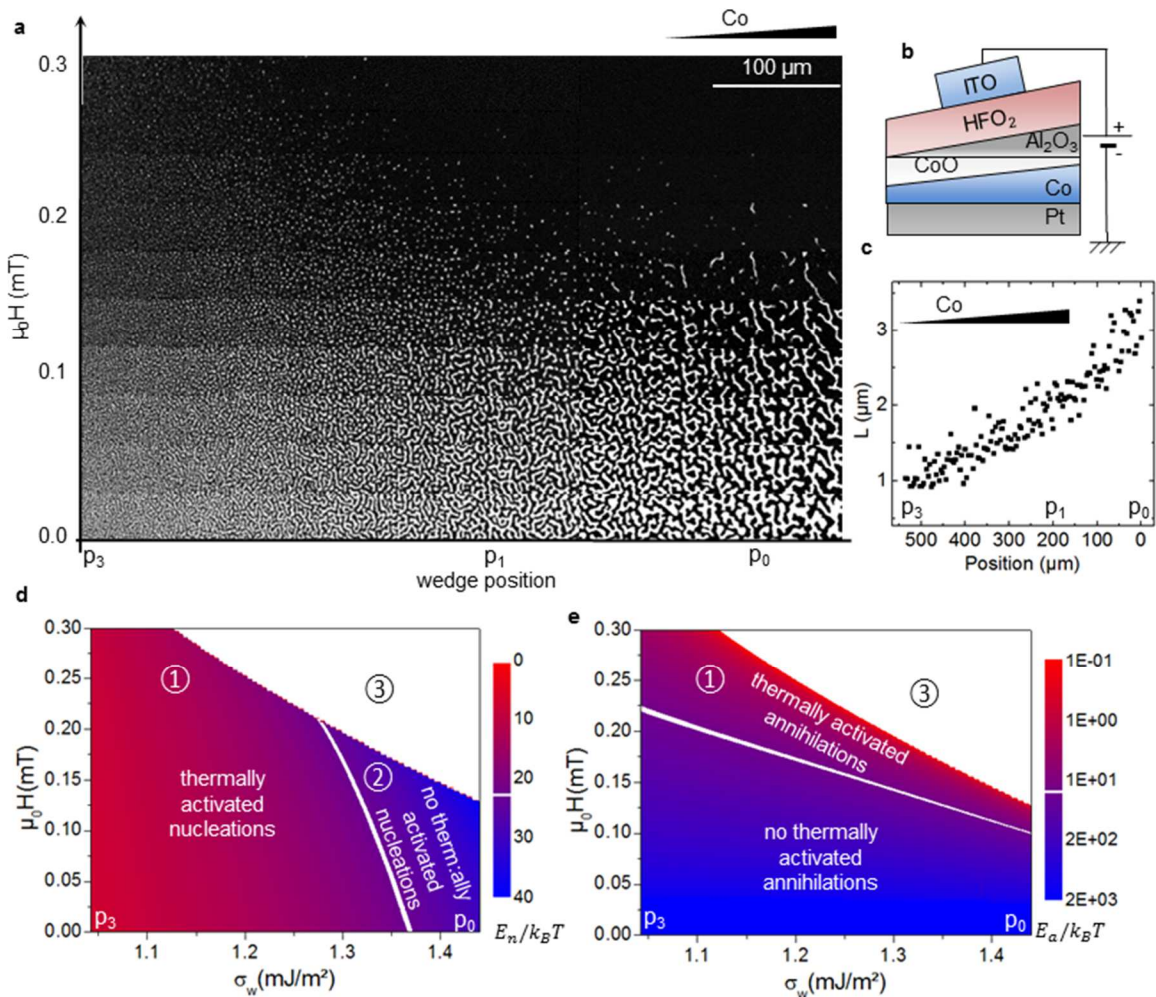


Figure 1: Labyrinthine and skyrmion bubble states. **a**, Polar Kerr magnetic images of the Pt/Co/oxide trilayer. The image is made of 10 images of $30 \times 550 \mu\text{m}$. Each image is recorded a few seconds after applying an out of plane magnetic field. The magnetic field was varied from 0 to 0.3 mT. The Co thickness is increasing from left to right. **b**, Schematic representation of the device: the Pt/Co/oxide trilayer is covered by a 90 nm HfO_2 layer and a top Indium Tin Oxide (ITO) electrode. **C**, Characteristic domain width L as function of the wedge position for zero applied magnetic field extracted by fast Fourier transform from **a**. **d** and **e**, Skyrmion bubble nucleation (**d**) and annihilation energies (**e**) calculated with the isolated bubble model as function of out of plane magnetic field and DW energy using the H , t , M_s and σ_w parameters estimated experimentally.

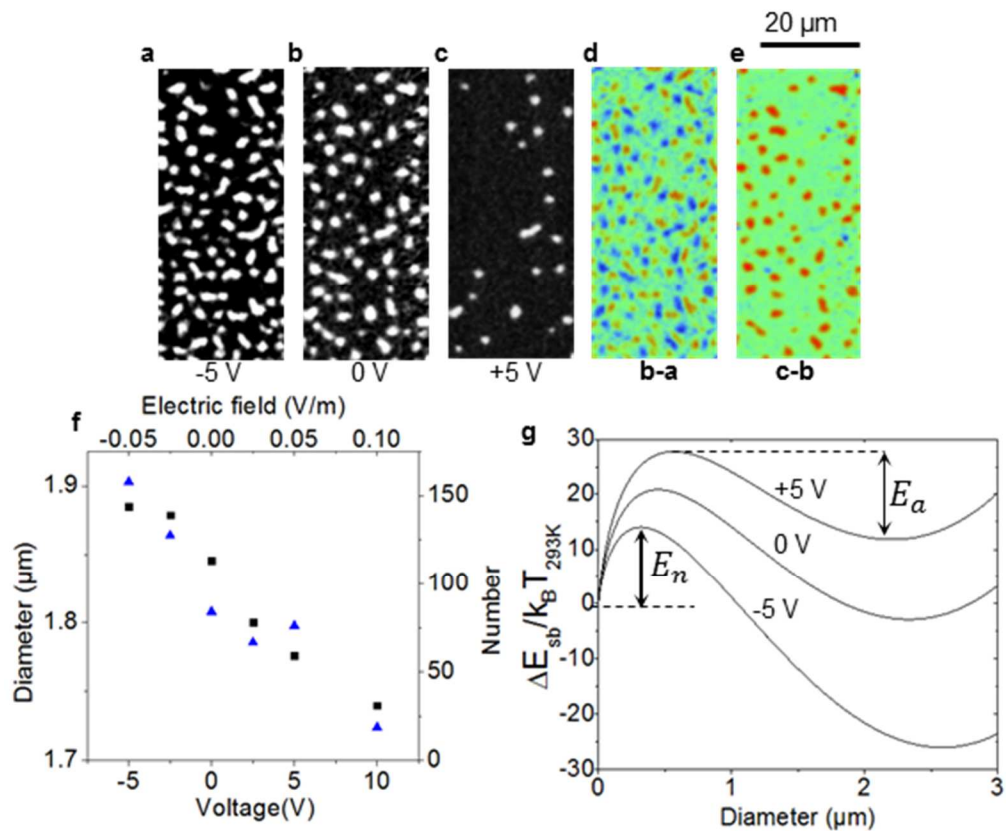


Figure 2: Electric field control of skyrmion bubbles density. **a** to **c**, Polar Kerr magnetic images of the Pt/Co/oxide trilayer under a static 0.15 mT perpendicular magnetic field, recorded through the transparent ITO electrode at position p_1 with different applied voltages. The sample is first saturated with a higher magnetic field, then the magnetic field is fixed to 0.15 mT and the electric field is varied from -5 V to $+10\text{ V}$. **d** and **e**, Differential images obtained from **b-a=d** and **c-b=e**. The blue/red bubbles correspond to objects which appeared/disappeared during the few seconds separating the images acquisition. **f**, Number and mean diameter of skyrmion bubbles extracted from images with twice the size of a,b and c. **g**, Analytical calculation of the energy difference between a saturated state and a single isolated magnetic bubble as function of the bubble diameter with the parameters $t = 0.468\text{ nm}$, $H = 0.15\text{ mT}$, $M_s = 0.92 + /- 0.05\text{ MA/m}$ and $\sigma_w = 1.33 + /- 0.17\text{ mJ/m}^2$. The t , H , M_s and σ_w parameters used for the simulation are determined experimentally.

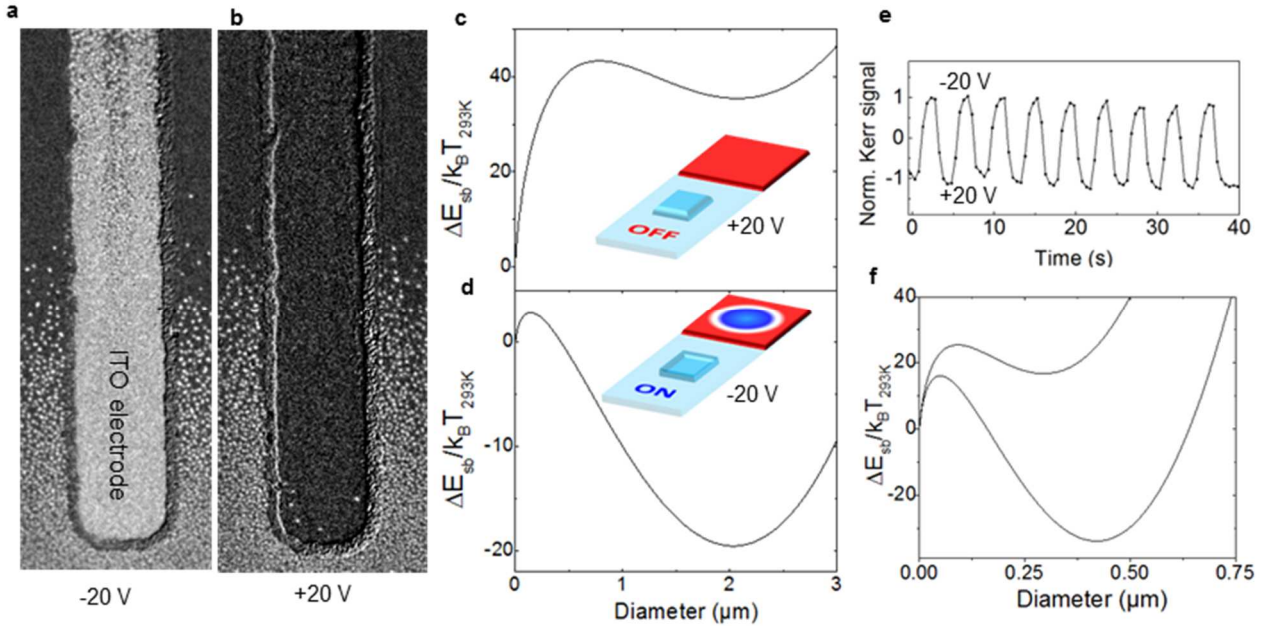


Figure 3: Electric field switching of skyrmion bubbles. **a and b**, Polar Kerr images of the Pt/Co/oxide thin film under a static 0.2 mT perpendicular magnetic field recorded 2 s after applying respectively -20 V and $+20\text{ V}$. **c and d**, Simulation of the skyrmion switch effect using an analytical isolated skyrmion bubble model with $t = 0.468\text{ nm}$, $H = 0.15\text{ mT}$, $M_s = 1.07\text{ MA/m}$ to 0.57 MA/m , $\sigma_w = 1.87\text{ mJ/m}^2$ to 0.45 mJ/m^2 **e**, Polar Kerr signal recorded through the electrode as function of time during a sequence of electric field switching from $+20\text{ V}$ to -20 V repeated every 2 s 10 times. **f**, Simulation of the skyrmion switch effect in the case of a thicker *Co* layer with the parameters $t = 0.6\text{ nm}$, $H = 0.9\text{ mT}$, $M_s = 1.3\text{ MA/m}$, $\sigma_w = 2.72\text{ mJ/m}^2$ and $\sigma_w = 2.57\text{ mJ/m}^2$.